



Texture imaging of zirconium based components by total neutron cross-section experiments

J.R. Santisteban^{a,*}, M.A. Vicente-Alvarez^a, P. Vizcaino^b, A.D. Banchik^b, S.C. Vogel^c, A.S. Tremsin^d, J.V. Vallerga^d, J.B. McPhate^d, E. Lehmann^e, W. Kockelmann^f

^a CONICET and Instituto Balseiro, Centro Atómico Bariloche, Argentina

^b Centro Atómico Ezeiza, Comisión Nacional de Energía Atómica, Buenos Aires, Argentina

^c LANSCE, Los Alamos National Laboratory, NM 87545, USA

^d University of California at Berkeley, Berkeley, CA 94720, USA

^e Paul Scherrer Institut, Villigen, Switzerland

^f Rutherford Appleton Laboratory, ISIS Facility, Chilton, OX11 0QX, UK

ARTICLE INFO

Article history:

Available online 7 July 2011

ABSTRACT

The transmission of thermal neutrons through an object is affected by the microstructure and crystallographic texture of the composing material. As a result, the total neutron cross section of common metallic objects departs largely from that expected for polycrystalline materials without preferred orientation. In this work we present the wavelength dependence of the total cross section of different Zr-based components of nuclear reactors, such as pressure tubes, rolled plates and welds. The experimental values found for the total cross section are discussed in terms of the crystallographic texture that results from the component manufacturing. The discussion is based on energy-resolved radiographies taken at the ISIS Facility, UK, using a novel micro-channel plate detector; and theoretical calculations of the elastic coherent total cross section from the orientation distribution function (ODF) of the crystallites composing a sample. The connection existing between texture and neutron transmission is exploited to investigate the spatial variation of texture across Zr-based components.

© 2011 Elsevier B.V. All rights reserved.

1. Introduction

The fabrication of structural components for nuclear power plants introduces characteristic crystallographic textures as a result of the thermo-mechanical processes involved during manufacturing. For Zr-based components, common deformation processes such as wire drawing, sheet rolling or tube reduction, produce a number of characteristic textures that have been extensively studied by Tenckhoff and co-workers [1]. Results show that the basal planes of the hexagonal unit cells and a $[1\ 0\ \bar{1}\ 0]$ direction are always parallel to the direction of the main deformation (e.g., the extrusion or rolling direction); whilst the basal poles primarily align to the direction of the effective compressive forces. So, the basal poles orient differently depending on the precise deformation conditions. In wire drawing the material is compressed concentrically, rendering basal poles randomly distributed around the wire axis. In rolling processes, the sheet is compressed in the normal direction while it is constrained in the transverse direction, resulting in basal poles preferentially parallel to the normal direction, but with a tendency to spread by $\pm 20^\circ$ to $\pm 40^\circ$ towards the transverse direction. Tubing is a complicated deformation process

with a triaxial stress-strain condition that depends on the specific fabrication technique. So different textures are found depending on the ratio $R = R_w/R_d$ between the reduction of wall thickness (R_w) to the reduction in diameter (R_d), which essentially compares the effective compressive forces in the radial and tangential directions respectively. For $R \sim 1$, both forces are similar and a fibre texture similar to that found in wire drawing is obtained, whilst for $R \gg 1$ the compressive normal forces are much stronger than the tangential ones, and typical sheet rolling textures are found. A different texture is found for $R \ll 1$, on which the basal poles align mainly along the tangential direction, but with a spread towards the radial direction. Texture gradients across specimens usually arise in these deformation processes due to differences in the forces operating on the outer and inner layers of the sheet, tube or wire. Moreover, texture gradients inevitably appear after welding of such components as a result of the high temperature gradients involved, which produces melting in the weld pool, and take the material in the heat affected zone (HAZ) through a double phase transformation (α - β - α). Hence on welding rolled plates the basal poles tend to align perpendicular to the weld line in the HAZ, whilst a rather isotropic texture is observed within the weld pool [2].

Neutron radiography is a well established imaging technique that achieves excellent contrast for hydrogen due to the large total

* Corresponding author. Tel.: +54 2944 445154; fax: +54 2944 445299.

E-mail address: J.R.Santisteban@cab.cnea.gov.ar (J.R. Santisteban).

cross section of the proton as compared to most other isotopes, particularly to those atoms composing structural nuclear materials. The dramatic changes that have occurred in neutron detection technology over the last years have furnished many neutron imaging instruments with energy/wavelength resolution [3–5]. Such energy resolution has opened new possibilities for the study of metal components, because the neutron transmission of polycrystalline materials presents sharp variations with neutron wavelength, which are very sensitive to the crystallographic texture of the material. It is the aim of this paper to study the spatial variations in texture that result from typical manufacturing processes of Zr components by performing *energy-dispersive* neutron radiography experiments on tubes, plates and welds of Zr-based alloys. The use of a radiographic technique is attractive because it offers good spatial resolution ($\sim 50 \mu\text{m}$), and it does not require sectioning of specimens, as usually required by conventional X-ray diffraction experiments. Besides this, we discuss the possibility of extracting quantitative information about the orientation distribution function (ODF) of the crystallites from the analysis of the neutron spectrum transmitted through a Zr-based specimen.

2. Total cross section of textured materials

On a first approximation, the transmission T of neutrons through a polycrystalline material of thickness x is:

$$T = \exp(-n\sigma_{\text{tot}}x) \quad (1)$$

where n is the number of unit cells per unit volume, with each cell having a neutron total cross section σ_{tot} . Fig. 1 displays the calculated total cross section of Zr powder for thermal and cold neutrons, indicating the different physical processes that contribute to the removal of neutrons from a collimated neutron beam. The calculation is based on the theoretical expressions discussed in Ref. [6]. Each neutron incident on the sample is either Bragg-reflected by a crystal plane, diffusely scattered, absorbed, or transmitted. At long wavelengths neutrons are removed from the beam mainly due to nuclear absorption, whilst at short wavelengths neutrons are scattered out of the beam by thermal diffuse scattering. Both contributions have a smooth dependence on neutron wavelength. For this wavelength range, absorption has a simple linear dependence on wavelength. Elements with large absorption, such as boron or cadmium, have long been exploited as contrast agents in neutron imaging. Thermal diffuse scattering, considered here as the combination of incoherent, low-angle, and inelastic thermal scattering, is large for hydrogenous materials and increases with the specimen temperature [6].

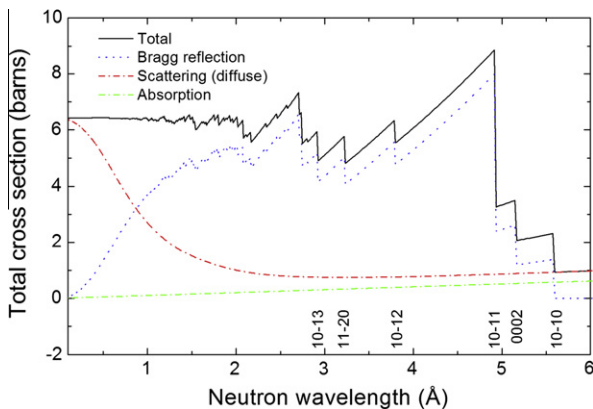


Fig. 1. Calculated total cross section for zirconium powder, identifying the different mechanisms removing neutrons from a collimated neutron beam. The sharp steps, called Bragg edges, indicate the cease of Bragg reflection on specific crystal plane families.

The increase of inelastic collisions at high neutron energies is responsible for the increase in diffuse scattering observed at short wavelengths. The sharp steps observed in the figure are the so-called *Bragg edges* and occur due to the reflection on the crystal planes. For a crystal family $\{hkl\}$, the Bragg angle increases as the wavelength increases, $\lambda = 2d_{hkl} \sin \theta$, until 2θ is equal to 180° . At wavelengths greater than $2d_{hkl}$ no Bragg reflection on this particular $\{hkl\}$ family can occur, resulting in a drop in the total cross section, i.e., a sharp increase in the transmitted intensity. The height of a Bragg edge (hkl) gives a direct measure of the number of crystallites having their $\{hkl\}$ planes normal to the incoming beam. The height of Bragg edges changes drastically for textured materials, and can even be absent along specific directions of a specimen. The total cross section due to Bragg reflection ($\sigma_{\text{coh}}^{\text{el}}$) along a specimen direction τ can be directly calculated from the pole figures $P_{hkl}^{\tau}(\alpha\beta)$ centred on τ [7]. As derived in that work, for neutrons of wavelength λ we need to count all the crystallites making the angle $\beta_{hkl} = (\pi/2) - \arcsin(\lambda/2d_{hkl})$ with the incident beam. This corresponds to the line integral of the pole figure $P_{hkl}^{\tau}(\alpha\beta)$ around a ring of radius β_{hkl} .

$$R(\tau, \lambda, d_{hkl}) = \int_0^{2\pi} P_{hkl}^{\tau} \left(\alpha, \pi/2 - \arcsin \frac{\lambda}{2d_{hkl}} \right) d\alpha \quad (2)$$

This factor corresponds to the *angular distribution function*, as defined in Ref. [29]. Hence, in order to calculate the total cross section along different sample directions, the pole figures need to be rotated accordingly. Using Eq. (2), the final expression for ($\sigma_{\text{coh}}^{\text{el}}$) for a textured material becomes

$$\sigma_{\text{coh}}^{\text{el}}(\tau, \lambda) = \frac{\lambda^2}{4V_0} \sum_{hkl}^{2d_{hkl} < \lambda} |F_{hkl}|^2 d_{hkl} R(\tau, \lambda, d_{hkl}) \quad (3)$$

where V_0 is the volume of the unit cell, and F_{hkl} is the structure factor. For an isotropic specimen $R(\tau, \lambda, d_{hkl}) = 1$, and we recover the expression for the elastic coherent total cross section given by Fermi et al. [8], which corresponds to the *Bragg reflection* total cross section plotted in Fig. 1.

3. Samples

Two different set of samples were used for these studies. One set consisted of small sections machined from commercial and experimental Zr2.5%Nb pressure tubes, whilst the other set corresponded to two Zircaloy-4 plates welded along their rolling direction.

3.1. Pressure tubes

Small sections having dimensions of $\sim 10 \text{ mm} \times 20 \text{ mm}$ along the axial and rolling directions, respectively, were machined out of Zr 2.5%Nb pressure tubes. Starting from Zr 2.5%Nb billets forged at $\sim 800^\circ\text{C}$, the normal fabrication route of CANDU pressure tubes performed for AECL (Atomic Energy of Canada, Ltd.) includes extrusion at $\sim 800^\circ\text{C}$, followed by air cooling, cold drawing to $\sim 20\text{--}30\%$ strain, and autoclaving at 400°C for 24 h. The microstructure of pressure tubes consists of α -grains up to about $10 \mu\text{m}$ long, $1 \mu\text{m}$ wide and $0.5 \mu\text{m}$ thick which have an *hcp* crystal structure containing between 0.6 and 1 wt% Nb, surrounded by a grain boundary network of Nb stabilized β -Zr, with a *bcc* crystal structure, that contains about 18–20 wt% Nb. The texture of the pressure tube is found to be determined at the extrusion stage [9] and, in principle, no relevant changes should be expected during cold drawing or annealing if performed at temperatures below the $\alpha/\alpha + \beta$ transus at 610°C .

One specimen, labelled as A, corresponds to the normal manufacturing process, and it was machined from a tube produced for

Table 1
Details of pressure tube samples studied in the present work.

Specimen	Label	Dimensions (mm)			(0 0 2) width (μe)
		Hoop	Axial	Radial	
A	Commercial	21.0	9.2	4.3	3600 \pm 200
B	Extruded	24.0	12.1	5.7	2000 \pm 100
C	Cold-rolled	21.4	11.8	4.1	10,700 \pm 800
D	Heat-treated	18.6	10.9	4.3	3300 \pm 200

the CANDU power plant at Embalse, Argentina. The other three specimens (B, C, D) were representative of different stages of an alternative manufacturing route for pressure tubes being developed at CNEA (Comisión Nacional de Energía Atómica), Argentina. The processing schedule being developed in Argentina starts from extruded tubes from a different supplier (Teledyne Wah Chang), and replaces the *cold drawing* stage by a pilger-type *cold rolling* stage [10]. Although the tube deformation introduced by cold drawing and cold rolling are equivalent (~ 20 – 30% strain), the differences in the starting material and between the cold deformation processes suggest that the dislocation density, residual stress and texture profile, resulting from both processes would not be the same. Specimen B corresponds to the 'as extruded' tube provided by Teledyne Wah Chang, specimen C was machined after 28% cold rolling, and specimen D was machined after 28% cold rolling and autoclaving at 400 °C for 24 h. Specific details about the specimens are presented in Table 1. Fig. 2 shows the (0 0 0 1), (1 0 1 0) and (1 0 1 1) pole figures for specimens A and C, which are averages through the full thickness and over a $300 \times 300 \mu\text{m}^2$ section of the samples. The pole figures are calculated from the ODF experimentally determined using the MTEX algorithm [11], from the analysis of full Debye rings recorded in synchrotron X-ray diffraction experiments with an 80 keV photon beam and a fast area detector [12]. The pole figures display the typical features observed in Zr2.5%Nb pressure tubes [9], which essentially shows the case of ratio $R \ll 1$ discussed in the previous section. The (0 0 0 2) basal planes present a pole along the hoop direction that elongates towards the radial direction, whilst the prismatic (1 0 1 0) planes show a strong pole along the axial direction. The number of grains with their *c*-axis pointing to the radial direction ~ 1.4 times random is still higher than for a randomly oriented polycrystal. Rather high texture indices (~ 7) give measure of the sharpness of these textures.

3.2. Welded Zircaloy-4 plates

Two plates of warm-rolled Zircaloy-4 plates of 6 mm thickness, produced by Wah Chang, USA (ASTM B352, Grade R60804) were TIG-welded along the plate rolling direction (RD). This weld reproduced the geometry of welds used for the manufacture of the reflector vessel for OPAL, a research reactor at ANSTO, Australia [13]. Fig. 3 shows the microstructure of the weld across the ND–TD plane, as observed in the microscope under polarized light, after polishing and etching of the samples following the procedures described in Ref. [14]. Different colours correspond to different grain orientations. On the top figure, vertical lines indicate the limits of the original (parent) material, of two distinct heat-affected zones (HAZ1 and HAZ2), and the weld pool. Details of the microstructure at different locations (a, b, c, d; in white in the photograph) are respectively shown by the pictures at the bottom. The original Zircaloy-4 plate has the typical equiaxed grain structure of annealed rolled plates, with diameters ranging from 10 to 20 μm . A thorough characterisation of this material has been presented in Ref. [15]. Drastic changes in microstructure occur across the HAZ of the weld. The temperature reached during welding is high enough to cause a phase change from the hexagonal α -phase into

the cubic (bcc) β -phase, followed by a return to the α -phase on cooling. These two phase-changes alter the grain shape and size, and the crystallographic texture from that of the original base plate. Two different HAZ's are identified in the figure, in order to distinguish the material that has experienced grain growth (HAZ1) from that which has not (HAZ2). The limit between both HAZ's corresponds to the vertical lines observed at ~ 10 mm from the weld centre, delimitating regions of different contrast. The sharp increase in grain size is appreciated in Fig. 3a, which shows the interface zone at a higher magnification. Towards the weld line, the microstructure of the HAZ1 consists of coarse, plate-like structures with irregular and jagged boundaries as seen in Fig. 3b, which have been called 'lenticular α ' in Ref. [16]. These coarse structures increase in size as the HAZ approaches the weld pool, reaching sizes of up to about 200 μm HAZ adjacent to the weld pool, see Fig. 3c. In the weld pool, the main feature consists of a central triangular region composed by 'basketweave' Widmanstatten structures [17], where the borders of the precursor β grains can be easily identified, Fig. 3d.

The crystallographic texture for the parent plate and for different locations of the HAZ was defined by neutron diffraction experiments performed at the HIPPO diffractometer of the LANSCE facility, USA [18]. For this purpose, small coupons, 2 mm along TD \times 4 mm along ND \times 6 mm along RD, were machined out of the weld from the locations indicated by the dotted rectangles on the right of Fig. 3. The experiments at HIPPO allowed the determination of the complete orientation distribution function (ODF) of the crystallites within the entire sample volume. The ODF for each coupon was defined from Rietveld-type least-squares analysis of the time-of-flight (TOF) spectra recorded along 99 sample directions, using the computer code GSAS [19]. Details about the texture analysis procedure together with results obtained for a PLASMA weld performed on the same material can be found in Ref. [20]. As observed in Fig. 4a, the original rolled plate (w1) presents a typical rolling texture, which can be idealized as being composed by two Zr grains having their *c*-axes lying on the ND–TD plane, at angles of $\pm 33^\circ$ to the ND. Essentially the same texture is observed for specimen w2, corresponding to the material within HAZ2. On the other hand, the ODF on the HAZ1 (specimens w3 and w4) present several texture components that result from the $\alpha \rightarrow \beta \rightarrow \alpha$ phase transformation occurring during welding [21]. The main additional texture component corresponds to Zr grains with their *c*-axis along the transverse direction, and (1 0 $\bar{1}$ 0) directions along the normal direction. This is a typical feature of welded zirconium-alloy plates with important technological implications, as this makes the HAZ more susceptible to delayed hydride cracking [22].

4. Testing

Energy-resolved neutron radiography experiments were performed on the ENGIN-X beamline at ISIS Facility, UK [23]. Short pulses of neutrons (~ 100 ns width) are created by bombarding a tungsten target with high-energy protons, 50 times per second. After passing through a liquid methane moderator, a polychromatic neutron beam illuminates the sample located at ~ 50 m from the moderator. An area detector placed just behind the sample registers both the position and time where the neutrons are detected. In this way, neutron radiographic images of the specimen are produced at different times, counted from the initial time t_0 when the original neutron pulse is produced. Neutrons emerging from the moderator with different energies will take different times (depending on their wavelength) to arrive at the detector. Therefore, each radiographic image taken for a specific time interval relative to the start time of the pulses reveals the transmission through the specimen for neutrons having a very precise energy.

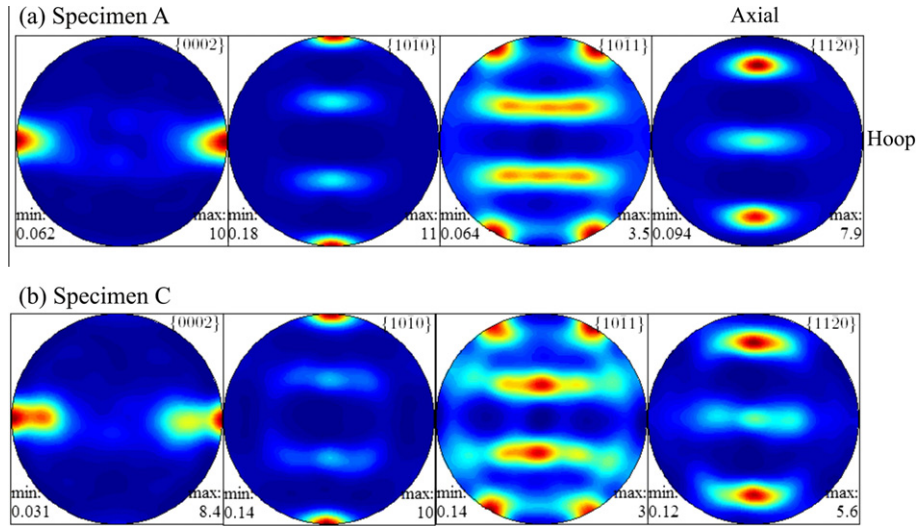


Fig. 2. Pole figures of Zr2.5%Nb pressure tubes studied in this work, determined by synchrotron X-ray diffraction [12]. (a) Commercial pressure tube and (b) Experimental pressure tube.

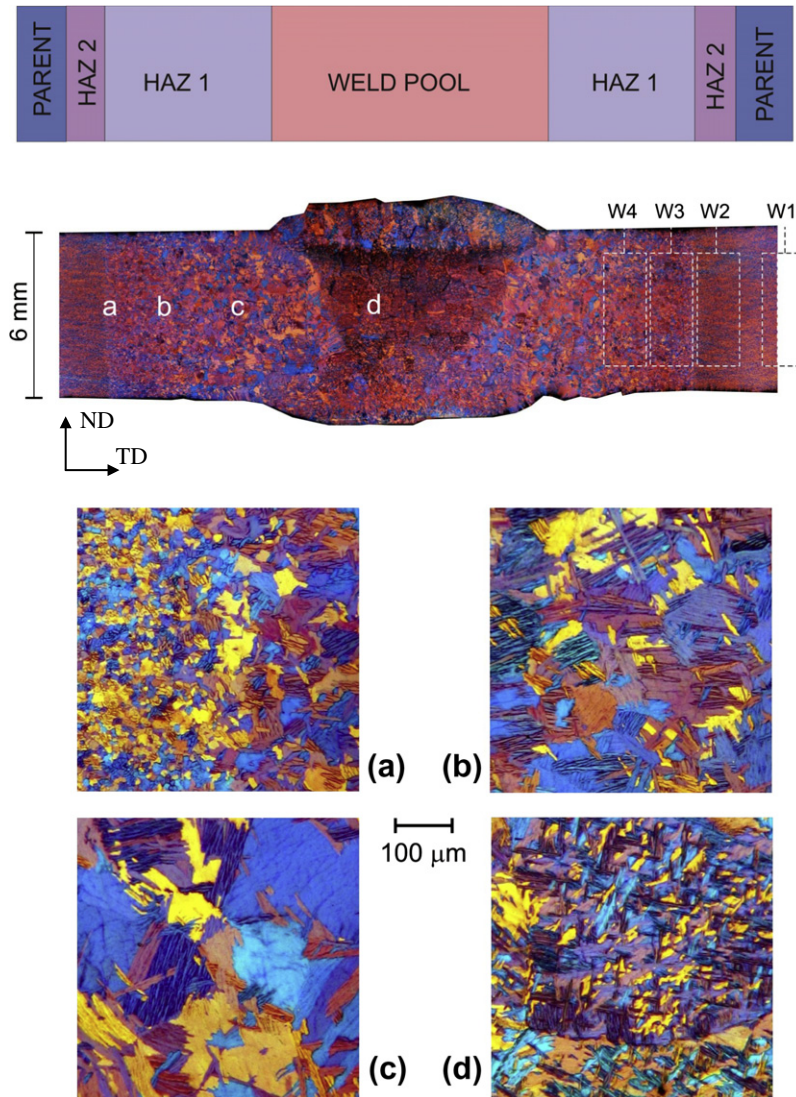


Fig. 3. Microstructure of TIG-welded Zircaloy-4 plates, from optical microscopy under polarized light. The top figure draws the limits of the original material, two distinct heat affected zones (HAZ), and the weld pool. The figures (a), (b), (c) and (d) show details at the locations indicated by corresponding white letters. The dotted rectangles labelled w1, w2, w3 and w4 represent the samples produced for texture analysis by neutron diffraction experiments.

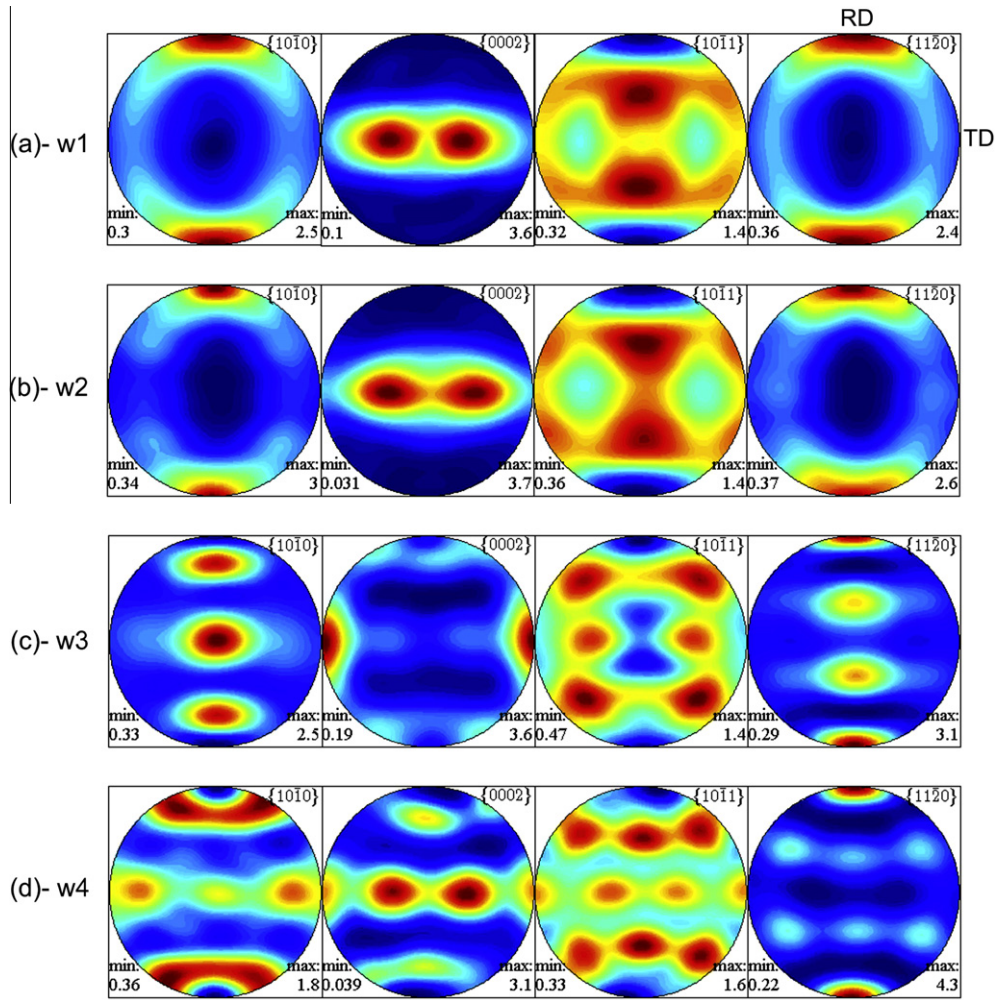


Fig. 4. Texture changes of Zircaloy-4 welded plates due to TIG welding. The pole figures correspond to samples taken from the locations indicated in Fig. 3, measured by neutron diffraction experiments performed at the HIPPO instrument, LANSCE, USA [20]. The large texture changes observed in the heat-affected zone HAZ1 (specimens w3 and w4) are due to the $\alpha \rightarrow \beta \rightarrow \alpha$ transformation experienced during welding.

The time-of-flight (TOF) that a neutron spends travelling the distance L from the moderator to the detector is more easily expressed in terms of its wavelength λ ,

$$TOF = \frac{m}{h} L \lambda \quad (4)$$

where m is the neutron mass and h the Plank constant. The use of a wavelength scale rather than an energy scale for the transmitted neutron spectrum allows direct comparison to the interplanar distances of the crystal lattice. Due to the low fluxes of neutron beams (as compared to electron or X-ray beams) each radiographic image is produced by adding the counts registered after several thousands of neutron pulses.

4.1. Detector description

In order to achieve energy-resolved radiography with a pulsed neutron source, a TOF resolution in the order of $10 \mu\text{s}$ and a spatial resolution in the order of $10 \mu\text{m}$ are required. In the present experiments this was achieved by a novel detector with a pixel size of $\sim 55 \mu\text{m}$ and a temporal resolution of $\sim 1 \mu\text{s}$, schematically shown in Fig. 5. The detector consists of a stack of microchannel plates (MCPs) coupled to a single readout application-specific integrated circuit (ASIC) [24]. Neutrons entering the detector are converted

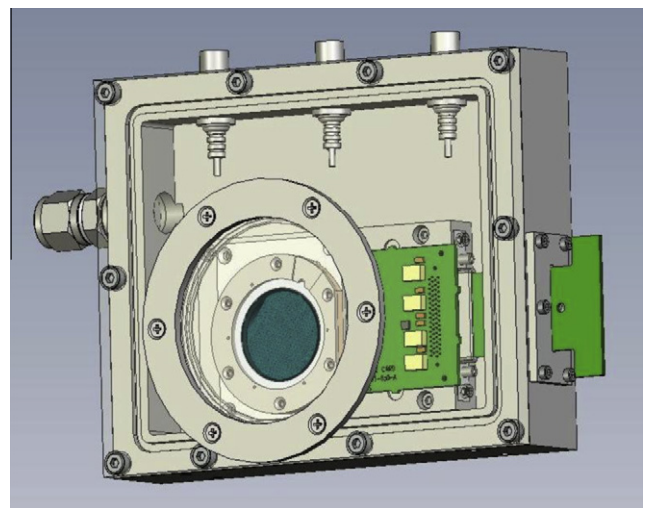


Fig. 5. Details of the prototype microchannel plate (MCP) detector used for the energy-resolved radiography experiments. The dark-green circular region indicates the neutron-sensitive boron-doped glass containing $8 \mu\text{m}$ holes (microchannels). The light-green plate is the application-specific integrated circuit (ASIC) that registers the electron pulses produced at the MCP.

into a large pulse of electrons by the MCPs (dark-green¹ in the figure), each of 33 mm diameter and ~0.8 mm thickness, densely packed with ~8 μm holes on an 11 μm pitch. The first MCP in the stack is doped with ¹⁰B atoms through its entire volume. The products of the neutron capture reaction (¹⁰B + n → ⁷Li + α) strike the walls of MCP pores, creating secondary electrons, which, in turn are multiplied in the pore adjacent to the point of neutron absorption. Hence, each pore of the MCP's operates as a secondary electron multiplier, providing gains of up to 10⁴ for a single stage [25]. The electron avalanche does not spread out, so the spatial information of neutron detection is preserved within a single pore. Two standard, i.e., non-neutron sensitive, MCPs are placed behind the ¹⁰B doped MCP for signal amplification, providing signal of 10⁴–10⁵ electrons for each detected neutron. The event amplification in MCP detectors happens within few nanoseconds, so the current time resolution (1 μs) is actually determined by the uncertainty in the location of the neutron absorption event, i.e., by the depth of the neutron absorber MCP (0.8 mm).

A Timepix readout ASIC with 55 × 55 μm² pixels is placed ~0.5 mm behind the MCP stack for detecting individual events once they are above the threshold level. The noise level of only ~75 erms in the Timepix pixels enables neutron counting with virtually no readout noise. The active area of the detector is 14 × 14 mm², limited by the area of the single readout ASIC. The efficiency of the detectors is close to 70% for cold neutrons and near 50% for thermal neutrons [25]. The counting rate capability of the detector (~100 KHz/cm²) is defined by the speed of the serial readout electronics. A rather coarse time of flight resolution of ~10 μs was sufficient for the present studies, yet several consecutive measurements using different TOF ranges were necessary in order to cover a wide range of neutron energies with this time resolution.

4.2. Experimental arrangement

In order to investigate texture gradients across the thickness of the pressure tubes, the four specimens (A, B, C, D) were stacked and placed directly in front of the detector, using two configurations. In Fig. 6a the specimens are arranged so that the incident neutron beam is parallel to the hoop direction of the tube; whilst in Fig. 6b the incident beam lies along the tube axial direction. The red arrows in both pictures indicate the direction of the neutron beam. As shown in Fig. 6c, an additional arrangement was used to study the wavelength dependence of the total cross section along the tube radial direction, with neutrons incident perpendicular to the page.

For the weld, radiographs were taken with the incident beam parallel to the weld line, i.e., perpendicular to ND–TD plane shown in Fig. 3.

The divergence of the incident neutron beam was 0.3° and the TOF range covered the interval 18,000–78,000 μs, which corresponds to a wavelength range between 1.42 and 6.15 Å. Typical counting times to achieve complete radiographic TOF spectra were 30 min.

5. Results

5.1. Results for pressure tube

Fig. 7 shows radiographs of the pressure tube specimens along different directions. The figures on the left correspond to radiographic images produced from the transmitted intensity $T(\lambda)$, integrated for wavelengths between 1.4 and 2 Å. This is a range where

¹ For interpretation of colour in Figs. 1–12, the reader is referred to the web version of this article.

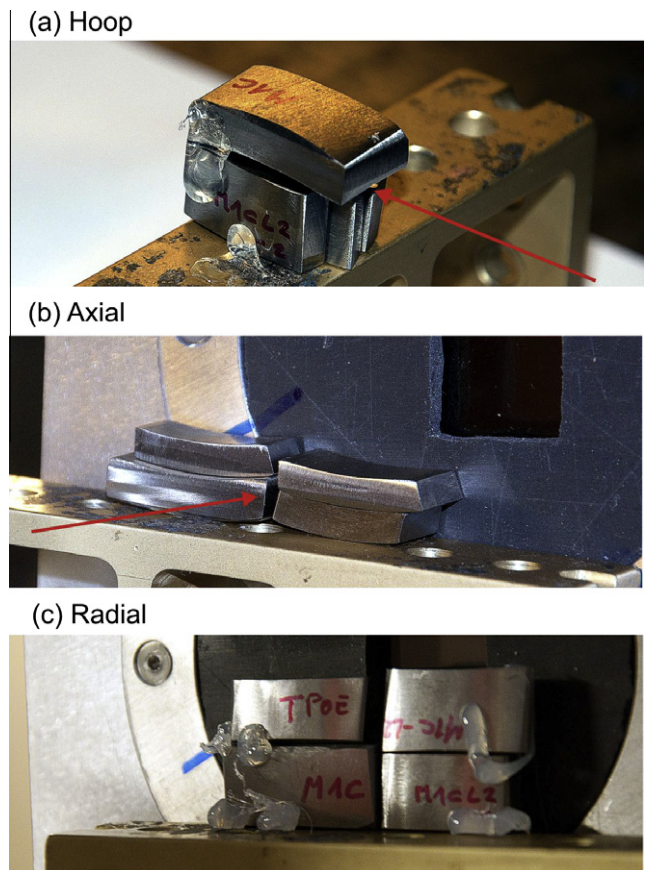


Fig. 6. Experimental arrangements used in the wavelength-resolved radiographies of the pressure tube specimens at the ENGIN-X beamline, Isis Facility, UK. The red arrows indicate the direction of the incident neutron beam. The MCP detector was always placed right behind the samples. The pictures show the different arrangements adopted to study the transmission along different directions of the tube.

the total cross section is densely populated by very small Bragg edges (Fig. 1). The counts registered at each pixel are normalized, i.e., they have been divided by the number of counts registered without the sample in the neutron beam. The silhouettes of the specimens are clearly distinguishable in the radiographs, so each specimen has been identified by its corresponding letter. The dark-blue shapes near the top-left and bottom-right corners in Fig. 7a correspond to the hydrogen-rich glue used to fix the specimens, which can be observed in Fig. 6a. On these *integral* radiographs, each sample presents a homogeneous light-blue tone; for both hoop and axial directions. The actual tone for each specimen is determined mainly by the thickness of the material traversed by the neutron beam, as inferred from Table 1. On the other hand, clear variations across some of the specimens are observed in the radiographs displayed on the right of Fig. 7, where the colour of a pixel is proportional to the intensity of selected Bragg edges. As a measure of the normalized height of a Bragg edge, we have adopted

$$I_{hkl} = \frac{\int_{2d_{hkl}-\Delta}^{2d_{hkl}+\Delta} T(\lambda) d\lambda - \int_{2d_{hkl}}^{2d_{hkl}+\Delta} T(\lambda) d\lambda}{\int_{2d_{hkl}-\Delta}^{2d_{hkl}+\Delta} T(\lambda) d\lambda} \quad (5)$$

The integration of the transmission T within the interval Δ on the wavelength scale is equivalent to an angular averaging around the direction of the incident beam. For the Bragg edge radiographs displayed in Fig. 7, we have adopted $\Delta \sim 0.04$ Å and $\Delta \sim 0.02$ Å respectively for the (0 0 2) and (1 0 1) Bragg edges, which corresponds to angular ranges of 7° and 5° around the specimen directions

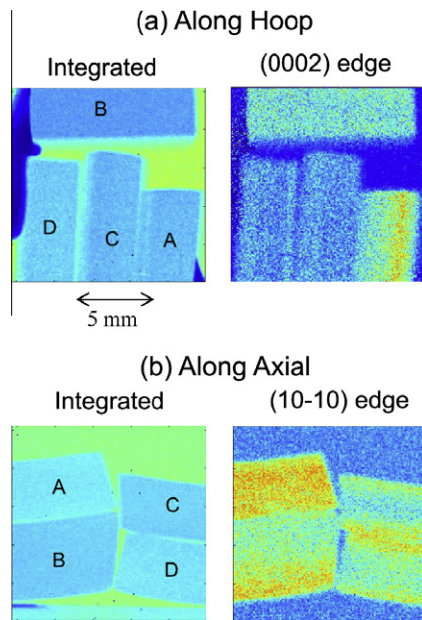


Fig. 7. Neutron radiographs of pressure tube specimens, for the two experimental arrangements displayed in Fig. 6a and b respectively. The radiographs on the left were produced from all transmitted neutrons with wavelengths between 1.4 and 2 Å. The letters identify the specimens listed in Table 1. The radiographs on the right are images of the height of Bragg edges, obtained from narrow wavelength ranges near the wavelengths indicated in Fig. 1. This reveals inhomogeneities of the manufacturing process that are invisible to neutron of other wavelengths.

quoted in the figure. Regarding the information provided by the (0002) Bragg edge along the hoop direction, a clear difference emerges between the inner and outer layers of specimen A, the commercial pressure tube. The inner (right) third of the tube thickness has about 40% more crystallites with their c axis along the hoop direction than the outer (left) third. Such difference was quantified by computing the total cross section for selected regions of this specimen, i.e., by adding the TOF spectra for pixels from selected regions of interest within the image. Similar gradients in texture are revealed by the (10 $\bar{1}$ 0) Bragg edge along the axial direction for the experimental pressure tubes. In this case, the outer layers of the extruded tube (specimen B) have a 25% increase in the number of crystallites with their (10 $\bar{1}$ 0) planes along the axial direction, whilst the cold-rolled and annealed tubes (specimens C and D) display differences only for a shallow 0.5 mm layer from the tube inner and outer surfaces. The physical origin of such variations in the transmitted intensity can be investigated by comparing the total cross section measured along different directions with theoretical predictions based on the equations discussed in Section 2. Fig. 8 shows experimental results (red dots) and calculations (blue lines) for specimen A along the axial, hoop and radial directions. The experimental values in figures (a) and (b) were derived from the TOF spectra obtained by adding the counts registered by the pixels within the region labelled as 'A' in Fig. 7a and b respectively. The experimental values in Fig. 8c were obtained using a transmission detector permanently installed on ENGIN-X [26], due to lack of allocated beam time during the experiments involving the MCP detector. The theoretical values in Fig. 8 were calculated via Eq. (3), from the pole figures presented in Fig. 2a. The line integrals involved in the calculation have been numerically performed using MTEX [11], an extremely powerful texture library developed in Matlab™. Large deviations are observed from the isotropic total cross section presented in Fig. 1 for all three directions; and a rather good agreement is found between experimental and calculated values. When comparing both curves, it must be remarked that there are no

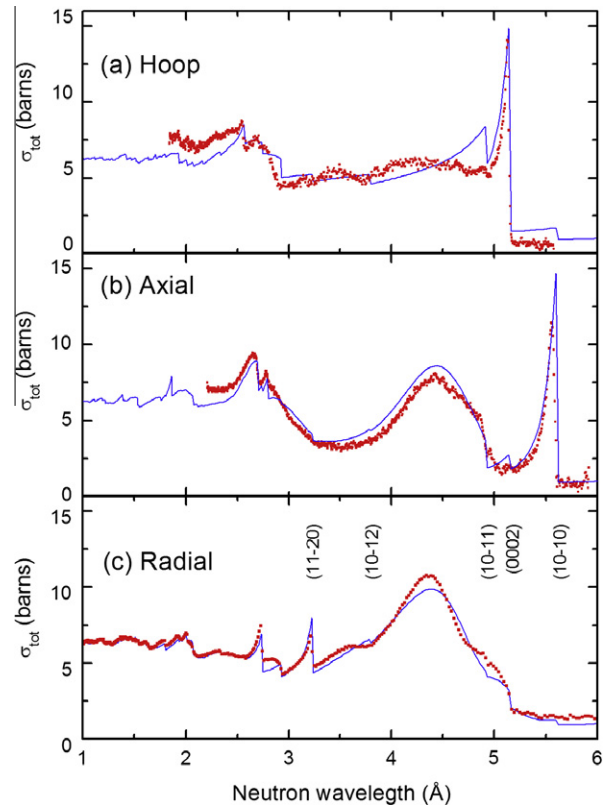


Fig. 8. Total cross section of pressure tube specimen A along different directions. Red dots are experimental values obtained from the transmitted TOF spectra measured on ENGIN-X, by combining the pixels corresponding to this specimen (see Fig. 7). Blue lines are theoretical values calculated from the pole figures presented in Fig. 2b. Large deviations are observed from the isotropic total cross section presented in Fig. 1.

adjustable parameters in the calculation and that the pole figures were obtained from a different experimental technique, i.e., synchrotron X-ray experiments using an area detector [12]. The large increase of the total cross section at the (10 $\bar{1}$ 0) Bragg edge along the axial direction, i.e., from a value of ~ 2 barns for the un-textured case up to a value of ~ 15 barns in the pressure tube is well captured by the calculation. This increase results from the very intense pole observed in the (10 $\bar{1}$ 0) pole figure presented in Fig. 2a. The same comment applies to the (0002) Bragg edge along the hoop direction. The poorest agreement between experiment and calculation is observed for the region to the left of the (10 $\bar{1}$ 1) edge along this direction.

As shown in Fig. 9, some differences are observed in the shape and height of the (0002) Bragg edges measured along the hoop direction for the different specimens. More remarkably, the cross section for the commercial specimen (A) is sharper and $\sim 40\%$ larger than for specimen C, in agreement with the pole figures displayed in Fig. 2. Only small differences are observed between the height of edges from specimens B, C and D which suggests that texture is not substantially affected by the cold rolling and autoclaving processes, in agreement with Ref. [9]. Yet, the different stages of the manufacturing process do manifest in the transmitted spectra through the broadening of the Bragg edges. Table 1 lists the width of the (0002) Bragg edges determined for the four specimens, obtained from least-squares fit to the edges using the analytic profile described in [26]. For proper interpretation, the edge width has been divided by the edge position, and so expressed in terms of microstrains ($1 \mu\epsilon = 10^{-6}$). The edge width of the experimental cold-rolled specimen (C, $10,700 \pm 800 \mu\epsilon$) is substantially

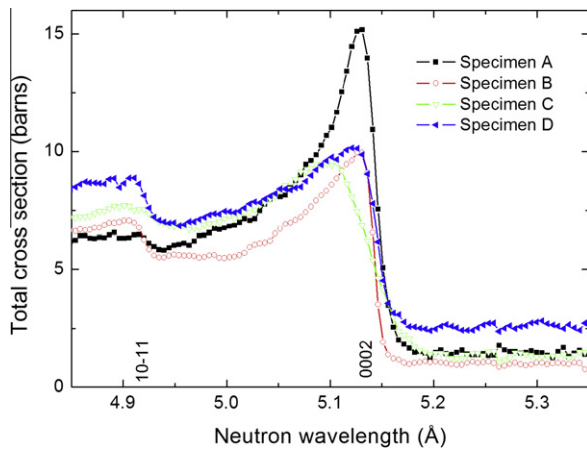


Fig. 9. Detail of total cross section along the hoop direction for the pressure tube specimens listed in Table 1. The (0002) Bragg edge of the commercial pressure tube (A) is 40% larger than the experimental ones. The rolled specimen (C) displays a much broader Bragg edge than the rest.

broader than the edge of the hot-extruded specimen (B, $2000 \pm 100 \mu\epsilon$), due to the large number of dislocations introduced by the deformation process. The autoclave process effectively relieves the stresses resulting from such deformation, which manifests through a considerably smaller width for the autoclaved specimen (D, $3300 \pm 200 \mu\epsilon$). This value is slightly lower than the edge width obtained for the commercial pressure tube (specimen A, $3600 \pm 200 \mu\epsilon$).

5.2. Results for Zircaloy-4 plate

Fig. 10 compares optical (a) and neutron radiography images (b, c, d, e) for the welded Zircaloy-4 plates taken with the neutron beam along the plates rolling direction. Figure (b) is a radiograph produced by integrating all the transmitted neutrons with wavelengths between 1.4 and 2 Å. Some bare contrast is distinguished in the image, but not clear connection can be established with the weld regions depicted in Fig. 3. On the other hand, figures (c), (d) and (e) show the radiographs obtained respectively from the intensity of the (10 $\bar{1}$ 0), (11 $\bar{2}$ 0) and (10 $\bar{1}$ 1) Bragg edges, using the edge intensity defined in Eq. (5). The limit of HAZ1 can be clearly identified in the (10 $\bar{1}$ 0) image, which suggests that the (10 $\bar{1}$ 0) pole observed in Fig. 4a and b quickly moves or disappears on entering the HAZ1. Fig. 10d indicates an increase of the intensity of the (11 $\bar{2}$ 0) pole across the HAZ1 on approaching to the weld pool. Observed in detail, the image also reveals a texture difference between the inner and surface regions of HAZ1 that can be connected to a difference in grain size revealed by optical microscopy. The (10 $\bar{1}$ 1) radiograph also reveals the start of HAZ1, but not as clearly as the (10 $\bar{1}$ 0) image; and shows some contrast between different regions of the weld.

As for the pressure tubes, some additional information can be gained by comparing the experimental and calculated total cross section for different locations of the welded plates, as displayed in Fig. 11. The experimental curves for the total cross section along the rolling direction shown in Fig. 11a were derived from the TOF spectra obtained by adding the pixels within the regions w1, w2, w3 and w4 shown in Fig. 3. The theoretical calculations for the total cross section along this direction were obtained via Eq. (3) using the experimental pole figures presented in Fig. 4. As before, the experimental total cross sections are markedly different from the isotropic cross section of Fig. 1. Overall, the absolute values and trends measured at different locations are well reproduced by

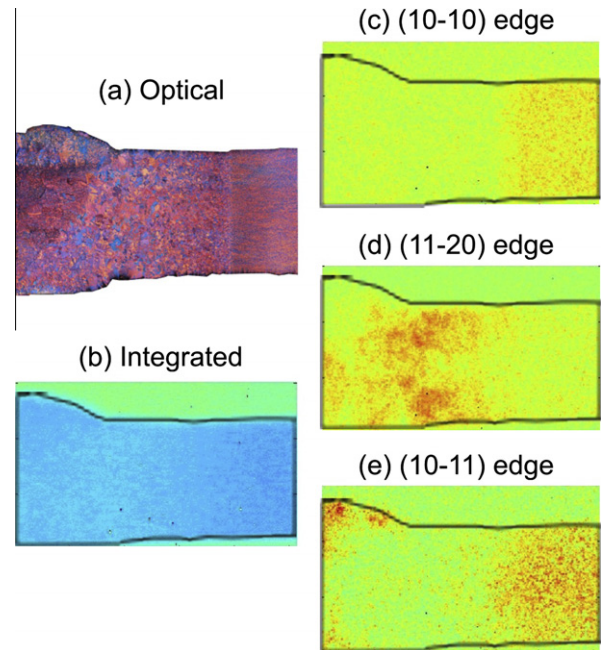


Fig. 10. Optical (a) and neutron radiography images (b, c, d, e) of the welded Zircaloy-4 plates. Figure (b) was produced from neutrons with wavelengths between 1.4 and 2 Å, whilst Figures (c), (d) and (e) are images of the height of selected Bragg edges. In figure (c) the start of HAZ1 clearly manifests through the disappearance of the (10 $\bar{1}$ 0) Bragg edges, whilst the (11 $\bar{2}$ 0) edge in figure (d) reveals the differences between the outer and inner layers of the plate.

the calculations. On a closer look however, we observed diverse levels of agreement for wavelength regions associated to different Bragg edges. The shape and sharp disappearance of the (10 $\bar{1}$ 0) Bragg edge when entering the HAZ1 is well captured by the calculation. A similar agreement is observed for the shape and increase in intensity of the (11 $\bar{2}$ 0) Bragg edge, whilst important differences between experiment and calculation are found for wavelengths between this edge and the (10 $\bar{1}$ 1) edge.

6. Discussion

The present experiments have shown that the wavelength variation of the total cross section for Zr 2.5%Nb pressure tubes (Fig. 8) and for rolled Zircaloy-4 plates (Fig. 11) departs considerably from the total cross section of an isotropic specimen (Fig. 1). The calculations performed here have proven that such changes can be effectively predicted through knowledge of the material ODF. To perform such calculations, we have used experimentally defined values for the ODF determined by high-energy X-ray diffraction (Fig. 2) and TOF neutron diffraction (Fig. 4). Moreover, the neutron radiographs presented in Figs. 7 and 10 have demonstrated the sensitivity of energy-resolved neutron imaging techniques to local variations in crystallographic texture within macroscopic components. Yet, much longer counting times would still be required to achieve high quality images with the energy discrimination strategy presented in this paper.

The computer libraries used to describe the neutron cross section of Zirconium alloys in reactor physics calculations always consider un-textured specimens [27]. However, the variations reported here are not expected to be of importance for such application, as the precise details of the orientation and energy dependence of the total cross section are lost at the group condensation stage. On the other hand, the observed variations in total cross section should be taken into account for neutron radiography determinations of hydrogen content [28].

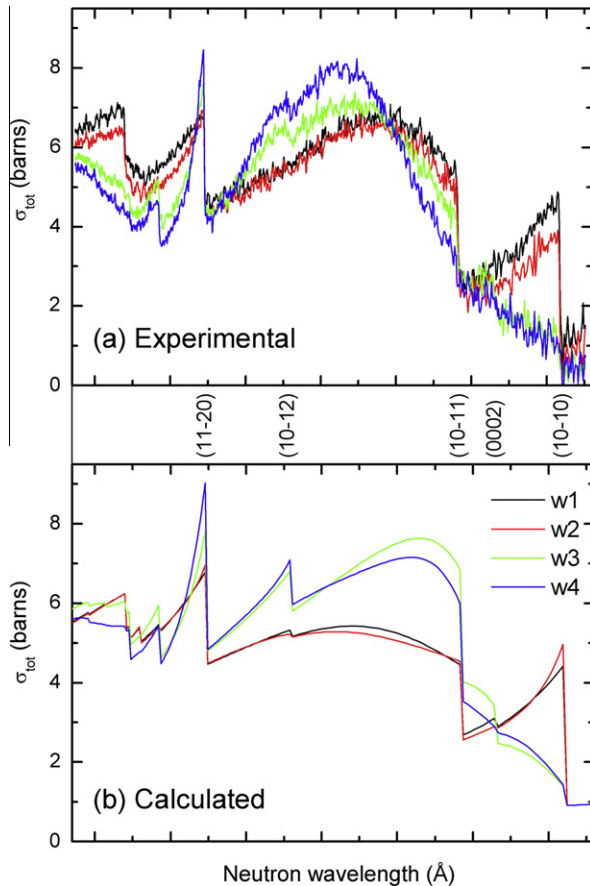


Fig. 11. Total cross section along the rolling direction, at different locations of welded Zircaloy-4 plates for the regions w1, w2, w3, w4 indicated in Fig. 3. (a) Experimental values obtained from the transmitted TOF spectra measured on ENGIN-X, by combining the pixels corresponding to each region (see Fig. 10); (b) Theoretical values calculated from the pole figures presented in Fig. 4.

Possible applications of the present results lie in the area of bulk materials characterisation. The crystallographic texture is a key property of Zr-based components of nuclear reactors due to its role on the irradiation-growth and creep to be experienced in service. The texture imaging capability presented here could be used as an aid for the optimization of manufacturing processes for such components. Moreover, the results in Figs. 8 and 11 demonstrate that in these Zr-based products the precise variation of the total cross section on neutron wavelength is very sensitive to the specimen orientation, and to the detailed structure of the ODF. This suggests the possibility of characterising the material ODF through measurements of the spectra transmitted along different directions. The determination of a completely unknown ODF would require the expansion of the ODF in terms of a suitable orthogonal base. In this sense, Bunge [29] has developed an expansion of the angular distribution function introduced in Eq. (2) in terms of Legendre polynomials, from which the ODF could be reconstructed in terms of a general spherical harmonics expansion. Along these ideas Vogel [30] has developed an analytic model for the total cross section of a material presenting a fibre texture, which has recently been applied to steel [31] and aluminium [32] specimens. On the other hand, for specific applications such as Zr-based plates or tubes, we could use a parametric model of the ODF made of a limited number of texture components. Such a model should contain the basic ingredients and characteristic features of the α -Zr ODF typically displayed by the component, in line with the information presented in the Introduction. We will consider the Zr 2.5%Nb pressure tubes to exemplify these ideas. In this case, the ODF is

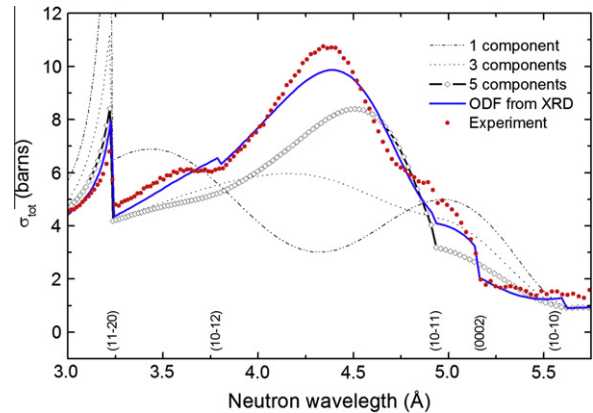


Fig. 12. Detail of total cross section of Zr2.5%Nb pressure tubes along the radial direction. The experimental values (red symbols) are compared with calculations obtained from an experimentally determined ODF (blue line) and from simple models including only a limited number of texture components (black lines).

composed by a strong texture component of grains having their c -axis pointing to the hoop direction and their $[10\bar{1}0]$ axis parallel to the axial direction; which are responsible for the strong (0002) and $(10\bar{1}0)$ poles observed in Fig. 2. This texture component can be represented by crystallites oriented mainly around two ideal orientations given by Euler angles $(\varphi_1, \varphi_2) = (90^\circ, 0, 0)$ and $(-90^\circ, 0, 0)$. However, the elongated structure of the (0002) pole towards the radial direction indicates that there are also a great number of grains with their $[10\bar{1}0]$ axis parallel to the axial direction but with their c -axis rotated from the hoop direction. In particular, in Fig. 2a the number of grains with their c -axis pointing to the radial direction (~ 1.4 times random) is still higher than for a perfectly isotropic polycrystal. These grains could be represented by adding a number of texture components with their c -axes along directions intermediate between the hoop and radial directions. A texture component rotated $+\varphi_i$ or $-\varphi_i$ from the radial direction can be described by ideal orientations with Euler angles $(\varphi_i, 0, 0)$ and $(-\varphi_i, 0, 0)$. Besides this, an additional texture component having their c axis along the axial direction could also be added in the model, in order to represent a small number of Widmanstatten-like α -grains directly transformed from the β -phase after extrusion [33]. In the analysis proposed here, the weight and angular width of each of these components could be refined from least-squares fits to the experimentally determined total cross section.

The sensitivity of the total cross section to different models for the ODF is illustrated in Fig. 12, comparing experimental (red symbols) and calculated values (lines) for the tube radial direction. Three synthetic models for the ODF (black lines), differing in the number of texture components included, are compared with the values calculated from the experimentally determined ODF (blue line). The calculations have been performed using the MTEX library [11] in Matlab™. A single texture component is clearly unable to reproduce the details of the experimental values. The increase in the number of texture components quickly tends to approximate the values of the much more elaborated ODF representation given by the blue line. It must be noted that the weights and widths of the texture components have not been refined; they are just educated guesses that produce acceptable pole figures. A unique width of 10° has been adopted for all components, and the weights have been equally distributed between the different components. The texture components have their c -axes at 10° intervals from the hoop direction (one component: hoop direction, three components: hoop, hoop- 10° , hoop- 20° , etc.). For all total cross sections presented through this paper, the major disagreement between experimental and calculated values is found for the wavelength

interval contained between the $(10\bar{1}1)$ and $(11\bar{2}0)$ Bragg edges. This region is dominated by the contribution from reflections on the $(10\bar{1}1)$ and $(10\bar{1}2)$ crystal planes. As it can be noted from Figs. 2 and 4, the $(10\bar{1}1)$ pole figures for tubes and plates are considerably more complex than for the other crystal families. In particular, some qualitative differences are even observed in the $(10\bar{1}1)$ pole figures of the commercial and experimental pressure tubes. So the calculation based on the line integral presented in Eq. (2) it is expected to be more difficult; and suggests that this contribution to the total cross section will be considerably more complex than those from other crystal planes.

7. Conclusions

Neutron transmission experiments have shown that the total cross section of Zr-based components of nuclear reactors is highly anisotropic over the thermal and cold energy ranges. This anisotropy is a direct manifestation of the crystallographic texture that results from the manufacturing processes. So, the dependence of the total cross section on neutron energy and on the component orientation can be directly calculated from the orientation distribution function (ODF) of the crystallites composing the material. Good agreement was found between experiments and calculations performed for Zr 2.5%Nb pressure tubes and welded Zircaloy-4 plates. Moreover, energy-resolved neutron radiography experiments revealed the spatial variation of the total cross section across these specimens, as a result of the inhomogeneous stress distributions that occur during manufacturing. As practical application for materials characterisation, we showed that a careful selection of neutron energy in neutron radiography can be exploited as a contrast agent to non-destructively reveal texture variations across Zr-based specimens.

Acknowledgments

This work was funded by research grants from ANPCYT-PICT672, Universidad Nacional de Cuyo 06/C325 and IAEA Research Contract 16024/R0. The authors would like to thank Axel Steuwer, and Anna Paradowska for their experimental help and fruitful discussions.

References

- [1] E. Tenckhoff, Deformation Mechanisms, Texture, and Anisotropy in Zirconium and Zircaloy, ASTM Special Technical Publication 966, Philadelphia, 1988.
- [2] J.H. Root, A. Salinas-Rodriguez, Textures and Microstructures 14–18 (1991) 989–994, doi:10.1155/TSM.14-18.989.
- [3] E.H. Lehmann, G. Frei, P. Vontobel, L. Josic, N. Kardjilov, A. Hilger, W. Kockelmann, A. Steuwer, Nuclear Instruments and Methods A603 (2009) 429–438, doi:10.1016/j.nima.2009.02.034.
- [4] W. Kockelmann, G. Frei, E.H. Lehmann, P. Vontobel, J.R. Santisteban, Nuclear Instruments and Methods A578 (2007) 421–434, doi:10.1016/j.nima.2009.02.034.
- [5] A. Tremsin, J.B. McPhate, W. Kockelmann, J.V. Vallerger, IEEE Trans. Nucl. Sci. 56 (2009) 2931–2936, doi:10.1109/TNS.2009.2029690.
- [6] W. Marshall, S.W. Lovesey, Theory of Thermal Neutron Scattering, Clarendon Press, Oxford, 1971.
- [7] J. R. Santisteban, L. Edwards, V. Stelmukh, Physica B 385–386 (2006) 636–638, doi:10.1016/j.physb.2006.06.090.
- [8] E. Fermi, W.J. Sturm, R.G. Sachs, Physical Review 71 (1947) 589–594, doi:10.1103/PhysRev.71.589.
- [9] R.A. Holt, S.A. Aldridge, J. Nucl. Mater. 135 (1985) 246–259, doi:10.1016/0022-3115(85)90084-4.
- [10] A.D. Banchik, D.R. Bianchi, P. Vizcaíno, A.V. Flores, W.C. Szieber, L.J. Galeta, A.G. Gómez, Technical report CNEA DD-ATN40MF-001, Tecnología de Fabricación de Componentes Estructurales del Núcleo base Circonio para Reactores Nucleares de Potencia, 2009 (in Spanish).
- [11] R. Hielscher, H. Schaeben, J. Appl. Crystallogr. 41 (2008) 1024–1037, doi:10.1107/S0021889808030112.
- [12] M.A. Vicente Alvarez, J.R. Santisteban, G. Domizzi, J. Almer, Acta Mater. 59 (2011) 2210–2220, doi:10.1016/j.actamat.2010.12.024.
- [13] D.G. Carr, M.I. Ripley, D.W. Brown, S.C. Vogel, T.M. Holden, J. Nucl. Mater. 359 (2006) 202–207, doi:10.1016/j.jnucmat.2006.08.021.
- [14] P.D. Kaufmann, P. Danielson, E.F. Baroch, ASTM STP 551 (1974) 52.
- [15] O. Zanellato, Ph D thesis, The Open University, United Kingdom, 2009.
- [16] O.T. Woo, K. Tangri, J. Nucl. Mater. 79 (1979) 83–94, doi:10.1016/0022-3115(79)90435-5.
- [17] R.A. Holt, J. Nucl. Mater. 35 (1970) 322–334, doi:10.1016/0022-3115(70)90216-3.
- [18] H.-R. Wenk, L. Lutterotti, S. Vogel, Nuclear Instruments and Methods in Physics Research A 515 (2003) 575–588, doi:10.1016/j.nima.2003.05.001.
- [19] R.B. Von Dreele, Journal of Applied Crystallography 30 (1997) 517–525, doi:10.1107/S0021889897000174.
- [20] J.R. Santisteban, P. Vizcaino, L. Fernandez, R. Samper, A.D. Banchik, S. Vogel, in: Proceedings 3rd Meeting of Asociación Argentina de Cristalografía, San Luis, 2007, ISBN: 978-987-1031-68-9 (CD ROM).
- [21] H.-R. Wenk, I. Lonardelli, D. Williams, Acta Mater. 52 (2004) 1899–1907.
- [22] C. Coleman, G. Doubt, R. Fong, J. Root, J. Bowden, S. Sagat, R. Webster, in: 10th Int. Symp. Zirconium Nuclear Industry, ASTM STP 1245: 264, 2004.
- [23] J.R. Santisteban, M.R. Daymond, L. Edwards, J.A. James, J. Appl. Crystallogr. 39 (2006) 812–825, doi:10.1107/S0021889806042245.
- [24] A.S. Tremsin, J.B. McPhate, J.V. Vallerger, O.H. Siegmund, J.S. Hull, W.B. Feller, E. Lehmann, Nuclear Instruments Methods in Physics Research A 604 (2009) 140–143.
- [25] A.S. Tremsin, W.B. Feller, R.G. Downing, Nuclear Instruments and Methods in Physics Research A 539 (2005) 278–311.
- [26] J.R. Santisteban, L. Edwards, M. E Fitzpatrick, A. Steuwer, P.J. Withers, M.R. Daymond, M.W. Johnson, N. Rhodes, E.M. Schooneveld, Nuclear Instruments and Methods in Physics Research Section A 481 (2002) 255–258.
- [27] R.E. MacFarlane, D.W. Muir, The NJOY nuclear data processing system, Version 91, Los Alamos National Laboratory, October 1994.
- [28] M. Grosse, G. Kuehne, M. Steinbrueck, E. Lehmann, J. Phys.: Condens. Matter 20 (2008) 104263, doi:10.1088/0953-8984/20/10/104263.
- [29] H.J. Bunge, Texture Analysis in Materials Science: Mathematical Methods, Butterworth, London, 1982.
- [30] S.C. Vogel, Ph D Thesis, Kiel University, Germany, 2000.
- [31] H. Sato, T. Kamiyama, K. Iwase, T. Ishigaki, Y. Kiyonagi, Nuclear Instruments and Methods A (2001) in press, doi:10.1016/j.nima.2011.01.063.
- [32] M. Boin, Ph D thesis, The Open University, United Kingdom, 2011.
- [33] R.A. Holt, P. Zhao, J. Nucl. Mater. 335 (2004) 520–528, doi:10.1016/j.jnucmat.2004.07.043.